



## Short communication

## Rational anode design for protonic ceramic fuel cells by a one-step phase inversion method

Jun Gao<sup>a</sup>, Yuqing Meng<sup>a</sup>, Tao Hong<sup>a</sup>, Sungkyu Kim<sup>a</sup>, Shiwoo Lee<sup>b,c</sup>, Kai He<sup>a</sup>, Kyle S. Brinkman<sup>a,b,\*</sup><sup>a</sup> Department of Materials Science and Engineering, Clemson University, Clemson, SC, 29634, USA<sup>b</sup> U.S. Department of Energy, National Energy Technology Laboratory, Morgantown, WV, 26507, USA<sup>c</sup> Leidos Research Support Team, Morgantown, WV, 26507, USA

## HIGHLIGHTS

- Developed one step phase inversion process with raw starting chemicals.
- Performance of phase inversion cell two times greater than conventional processing.
- Improvements attributed to enhanced polarization resistance of anode.

## ARTICLE INFO

## Keywords:

Protonic ceramic fuel cell  
Phase inversion

## ABSTRACT

A one-step phase inversion method was applied to fabricate an optimized anode structure for protonic ceramic fuel cells (PCFCs). The phase inversion process utilized raw starting chemicals, instead of crystalline BaCe<sub>0.7</sub>Zr<sub>0.1</sub>Y<sub>0.1</sub>Yb<sub>0.1</sub>O<sub>3-δ</sub> (BCZYYb) powder in an energy and time saving process. The resulting large and fingerlike pores exhibited enhanced performance as compared to the disordered pores produced by conventional preparation of anode structures using dry pressing methods. The electrochemical performance of the rational designed anode supported cell were 491, 402, 302 and 200 mW cm<sup>-2</sup> at 700, 650, 600 and 550 °C, respectively, which was nearly twice than the cell with dry pressing anode. An equivalent circuit modeling method was used to separate the anode polarization resistance from the single cell, confirming that the overall cell performance improvements were attributed to microstructural modifications of the anode by the phase inversion process. The one-step phase inversion method demonstrated great promise for improved processing of fuel cells and separation membranes.

## 1. Introduction

Solid oxide fuel cells (SOFCs) have received significant attentions in sustainable energy systems due to their high efficiency, fuel flexibility and limited by-products [1–5]. Compared to the traditional oxygen-ion based SOFCs, protonic ceramic fuel cells (PCFCs) based on the proton conducting ceramics have a lower activation energy, which results in the potential to be used at lower temperatures (below 700 °C) [6–9].

Recently, extensive efforts have been devoted to improving the performance of SOFCs by designing nano-structured electrodes. The most useful strategy is by infiltration ionic conducting materials, mixed ionic-electronic conductor (MIEC) or catalysts in the electrode backbone to achieve a nano-structure electrode. For example, Chen et al. developed a dual-phase cathode, composed of perovskite PrNi<sub>0.5</sub>Mn<sub>0.5</sub>O<sub>3</sub> (PNM) and exsolved fluorite PrO<sub>x</sub> particles. The

cathode area-specific resistance was 0.052 Ω cm<sup>2</sup> at 700 °C and showed remarkable long-term stability [10]. Hua et al. [11] infiltrated PrBaMn<sub>2</sub>O<sub>5+δ</sub> combined with a nanosized Ni<sub>4</sub>Co bimetallic catalyst in BaCe<sub>0.7</sub>Zr<sub>0.1</sub>Y<sub>0.1</sub>Yb<sub>0.1</sub>O<sub>3-δ</sub> (BCZYYb) porous anode backbone. The resulting fuel cells demonstrated remarkable sulfur resistance and in situ methane reforming due to the nanoarchitecture in the anode of PCFCs. In addition to composition, the microstructure of electrodes plays an important role in cell's performance. Jihwn An et al. [12] successfully developed a three-dimensional (3-D) SOFC architecture, achieving a peak power density of 1.3 W cm<sup>-2</sup> at 450 °C with ultrathin (60 nm) electrolyte. Toshio Suzuki found that higher linear fuel velocity led to better cell performance with higher anode porosity [13].

Many methods have been attempted to fabricate highly porous electrode structures including tape casting [14,15] and dry pressing [16]. The use of starch or graphite as the pore former typically results in

\* Corresponding author. Department of Materials Science and Engineering, Clemson University, Clemson, SC, 29634, USA.

E-mail address: [ksbrink@clemson.edu](mailto:ksbrink@clemson.edu) (K.S. Brinkman).

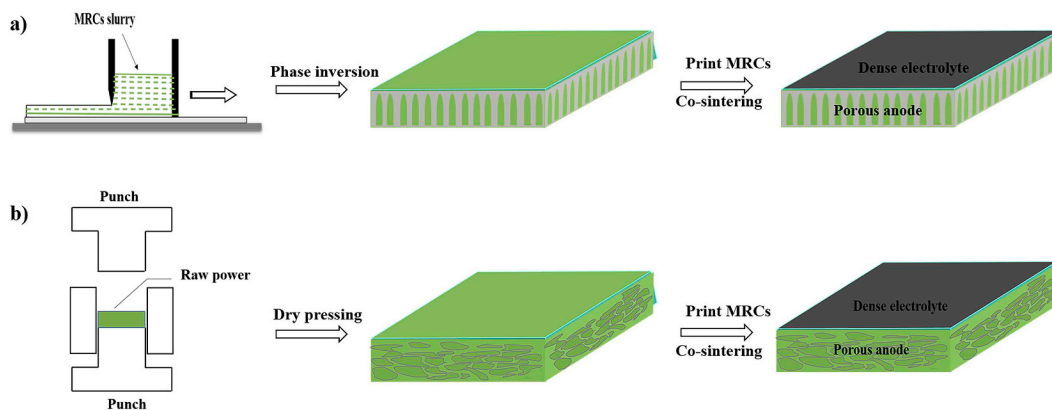


Fig. 1. Schematic diagram of the anode supported thin film half-cell preparation route with a) one-step phase inversion process and b) traditional dry pressing process.

a tortuous pore structure which does not facilitate gas transport in the electrodes. Another promising method is phase inversion [17–21], the formed fingerlike pores were perpendicular to the electrolyte, which are favorable for gas transport. Shi et al. [22] reported a Ni-BaZr<sub>0.3</sub>Ce<sub>0.5</sub>Y<sub>0.2</sub>O<sub>3-δ</sub> anode substrate by phase inversion method, demonstrating good electrochemical performance with peak power densities of 455 mW cm<sup>-2</sup> measured at 600 °C, much higher than those of the traditional dry-pressing cells.

However, the typical phase inversion method to fabricate the anode substrates or membranes include multiple steps of powder synthesis through solid state reaction method or wet-chemistry routes. This process is time and energy-consuming, and results in toxic gases (e.g. NO<sub>x</sub>) emissions. Zhu et al. [23] used one-step thermal processing to precisely controlled cation stoichiometry in perovskite hollow Ba<sub>0.5</sub>Sr<sub>0.5</sub>Co<sub>0.8</sub>Fe<sub>0.2</sub>O<sub>3-δ</sub> fibers, exhibiting high oxygen permeation flux values.

Herein, we proposed a one-step phase inversion method to fabricate the anode substrate in PCFCs. Instead of using crystalline BCZYYb powder, we began with the raw chemicals-oxides and carbonates for the phase inversion process. The NiO-BCZYYb crystal phase formed at high temperatures during the co-sintering process with the electrolyte. The rational designed anode microstructure and electrochemical performance were characterized and compared with the dry pressing anode supported cells. The results show that excellent performance was achieved by using the one-step phase inversion method to fabricate the anode supported PCFCs.

## 2. Experimental

### 2.1. Power synthesis

La<sub>0.6</sub>Sr<sub>0.4</sub>Co<sub>0.2</sub>Fe<sub>0.8</sub>O<sub>3-δ</sub> (LSCF) powder was synthesized by the combustion method [24]. Stoichiometric amounts of precursors La(NO<sub>3</sub>)<sub>3</sub>, Sr(NO<sub>3</sub>)<sub>2</sub>, Co(NO<sub>3</sub>)<sub>3</sub>, and Fe(NO<sub>3</sub>)<sub>3</sub> (99.5%, Sinopharm Chemical Reagent Co.) were dissolved in distilled water, then the citric acid and ethylenediaminetetraacetic acid (EDTA) were added to the solution with metal/citric acid/EDTA ratio of 1:1:1, working as the chelating agent to assist the combustion process. The precursor solution was heated on a hot plate to form a gel and then calcinated at 800 °C for 2 h to remove organic residue from the ash to obtain a pure phase LSCF.

### 2.2. Preparation of single cells

The rationally designed 40 wt% BCZYYb + 60% wt.% NiO anode was fabricated by using the new one-step phase inversion tape casting method. In particular, mixed raw chemicals (MRCs) instead of BCZYYb powder were used for the phase inversion process. Stoichiometric

amounts of BaCO<sub>3</sub>, CeO<sub>2</sub>, ZrO<sub>2</sub>, Y<sub>2</sub>O<sub>3</sub>, Yb<sub>2</sub>O<sub>3</sub> and NiO were mixed and stirred with polyvinylpyrrolidone (PVP) as the dispersant and polyethersulfone (PESf) as the binder in N-methyl-2-pyrrolidone (NMP) solution in a rolling mill for 24 h. The slurry then casted onto a Mylar substrate with blade height of 1 mm and transferred into water bath for 12 h for solidification via the phase inversion process. This was followed by drying the green tape at room temperature for 12h. Finally, the green tape was punched to pellets with diameter of 19 mm to obtain the final anode structure.

For comparison, the dry pressing method was used to obtain green anode with different pore structures with the same composition. Stoichiometric amounts of BaCO<sub>3</sub>, CeO<sub>2</sub>, ZrO<sub>2</sub>, Y<sub>2</sub>O<sub>3</sub>, Yb<sub>2</sub>O<sub>3</sub>, NiO and starch were mixed together in isopropanol with 3-mm yttria-stabilized zirconia (YSZ) beads for 48h, followed by drying at 90 °C for 24h. The pellets were dry-pressed under 160 Mpa for 1 min in a circular carbon-aided steel die with diameter of 19 mm to produce the green anode.

The BCZYYb electrolyte precursor powder was prepared by mixing stoichiometric amounts of BaCO<sub>3</sub>, CeO<sub>2</sub>, ZrO<sub>2</sub>, Y<sub>2</sub>O<sub>3</sub> and Yb<sub>2</sub>O<sub>3</sub> with addition of 1.0 wt% NiO as the sintering aid together in isopropanol with the same mixing and drying process with the dry pressing anode precursor powder. A mixture of the electrolyte precursor powder with binder and dispersant to form the electrolyte slurry was then deposited on the skin layer side of the anode and any side of the dry pressing anode. Finally, the materials were co-sintered at 1450 °C for 12 h to obtain the half cell, as illustrated in Fig. 1.

### 2.3. Characterization and testing

The crystalline structure of the samples was using X-ray diffraction (XRD, Rigaku TTR-III diffractometer) with Cu Kα radiation source. The XRD patterns were obtained in the range of 20°–80° with a 0.02° step size and a scan speed of 0.5°/min. The cell structure was examined using scanning electron microscopy (SEM, Hitachi S-4800) and transmission electron microscopy (TEM, JEOL JEM-2100F). The microstructure of the anode/electrolyte interface with related elements compositions were studied using scanning transmission electron microscopy (STEM) combined with energy dispersive X-ray spectroscopy (EDS). The density of the samples was measured using Archimedes method, and the porosity was calculated from  $(1 - \rho/\rho_{th}) \times 100\%$ , where  $\rho_{th}$  is the theoretically density of the anode (60 wt% NiO-40 wt% BCZYYb).

Anode supported single cells were sealed in an aluminum tube by ceramic bond, and the silver wires were used as the voltage and current leads on both sides. The electrochemical performance of single cells was evaluated by using the humidified (3% H<sub>2</sub>O) hydrogen as the fuel and the ambient air as the oxidant. Electrochemical impedance spectra were obtained using an electrochemical workstation (Solartron®, SI

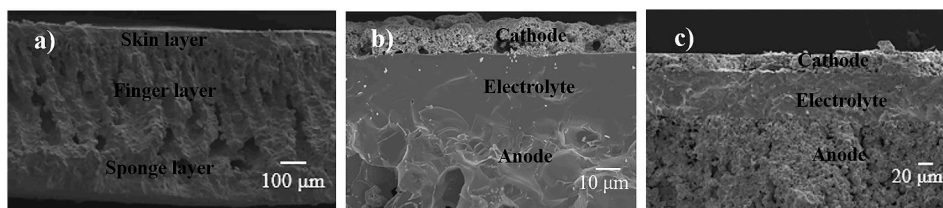


Fig. 2. a) SEM of tri-layered structure rationally designed anode, b) single cell with one-step phase inversion anode and c) single cell with traditional dry pressing anode.

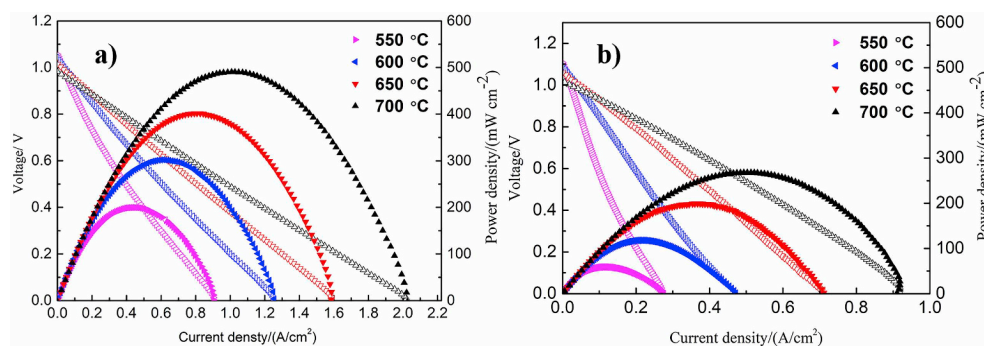


Fig. 3. Voltage and powder density versus current density for single cells with a) one-step phase inversion anode and b) traditional dry pressing anode.

1287 + 1260) with an AC amplitude of 10 mV in the frequency range from 1 MHz to 10 MHz. AC impedance plots were fitted by using Zview software according to the equivalent circuit.

### 3. Results

#### 3.1. Single cell microstructure

The crystalline structure of the anodes after co-sintering was confirmed by the XRD patterns, shown in Fig. S1. The XRD patterns of the rationally designed anode and traditional anode are similar, indicating that the BCZYYb forming during the one-step phase inversion process was consistent with the observations in the traditional solid-state reaction method. In addition, no other phases were found to form during this process, which indicates no loss of the metal ions and no significant interactions during the one-step phase inversion process.

Fig. 2a and b displays the SEM micrograph of the resulting rationally designed anode with a tri-layered structure including a skin layer, a fingerlike porous layer, and the sponge layer. The skin layer adjacent to the dense electrolyte exhibited a fine microstructure with reduced pore sizes, which could increase the density of the triple-phase boundaries along electrode/electrolyte interface. Moreover, the large fingerlike pores were vertical to the electrolyte, which should improve the gas transport and decrease the concentration resistance. And the overall porosity of the anode was 55.1%. In comparison, Fig. 2c shows the SEM micrograph of the tri-layered single cell with traditional anode, showing randomly pore distribution with a lower porosity (32.6%). In particular, gas transport resistance could be increased due to the pores parallel to the electrolyte direction and that not all pores are connected with each other. In addition, the dense electrolyte was nearly 40 μm thick, which indicates a high open voltage for the single cell. Also, in Fig. S2, after reduction, a uniform distribution of Ni and BCZYYb grains in the anode, without cracks and providing a uniform distribution of TPBs in both phase inversion anode and dry pressing anode. Furthermore, the phase inversion anode keeps the original asymmetrical structure well with larger porosity, allowing fast gas transport.

Fig. S3 compares the STEM images of the anode/electrolyte interface for cells with a one-step phase inversion anode and dry pressing anode. As displayed in Figs. S3a and S3b, the electrolyte is highly dense with good interfacial contact between the anode/electrolyte. A notable difference between the anode/electrolyte interface in the phase

inversion versus the dry pressed sample is the larger NiO grains present at the interface in the phase inversion anode. After reduction, this should result in increased triple phase boundaries and be beneficial to the chemical reactions occurring at the interface. The high-resolution TEM (HRTEM) images and corresponding electron diffraction patterns of the BCZYYb and NiO phases at the interface are displayed in Figs. S3c and S3d, respectively.

Figs. S4a and S4b shows the element distribution of the BCZYYb at the interface, which is quantitatively summarized in Table S1. The BCZYYb phase from both anodes have a similar composition as compared with the target composition. This indicates that phase formation of the BCZYYb in the one-step phase inversion method occurs in a similar manner to the conventional sintering process.

#### 3.2. Single cell performance

Fig. 3 shows the typical cell voltage (V) and power density (P) results as a function of the current density (J). The open circuit voltage is close to the theoretical value (1.1V), corresponding to the dense electrolyte in SEM of both cells. The maximum power density of the single cell with traditional dry pressing anode in our previous work [25] was 268, 199, 118 and 58 mW cm<sup>-2</sup> at 700, 650, 600 and 550 °C, respectively. These results are comparable to the literature with LSCF as the cathode in PCFCs. For example, Shang [26] reported Ni-BCZYYb/BCZYYb/LSCF single cell with a maximum power density of around 150 and 110 mW cm<sup>-2</sup> at 650 and 600 °C respectively. The maximum power density nearly doubles by using the rationally designed anode, especially at lower temperatures, reaching 491, 402, 302 and 200 mW cm<sup>-2</sup> at 700, 650, 600 and 550 °C, respectively. It is emphasized that these samples employ the same electrolyte, cathode and the same composition of the anode, therefore the improvements in the performance must be attributed to the microstructure modifications in the anode.

Table 1 summarizes the performance of recently published PCFCs with LSCF various cathodes employed in literature. A comparison of our cells to the existing literature of PCFCs with LSCF cathodes indicates that the one-step phase inversion method for anode fabrication results in a higher powder density than the corresponding full cells where the anode was fabricated by the dry pressing method. The performance of the full cell in this work is slightly lower than the best reported power density with phase inversion anode due to the difference of the thickness of electrolyte [22]. Assuming similar losses at the electrodes and

**Table 1**  
Summary of output performance (humid hydrogen) of PCFCs in literature.

Anode	Cathode	Electrolyte	Electrolyte thickness( $\mu\text{m}$ )	Power density ( $\text{mW cm}^{-2}$ )	Ref
NiO-BCZY535 Dry pressing	LSCF-BCZY535	BCZY1	8	231 (600 $^{\circ}$ C)	[27]
NiO-BZY20 Dry pressing	LSCF	BZY20	15	172 (600 $^{\circ}$ C)	[28]
NiO-BCZYYb Dry pressing	LSCF	BCZYYb	60	110 (600 $^{\circ}$ C)	[26]
NiO-BCZYYb Dry pressing	BCZYYb-BCFZY (infiltration)	BCZYYb	30	455 (500 $^{\circ}$ C)	[29]
NiO-BCZY17 Phase inversion	SSC-SDC	BCZY17	25	55 (600 $^{\circ}$ C)	[30]
NiO-BCZY35 Phase inversion	LSCF-BCZY35	BCZY35	14	455 (600 $^{\circ}$ C)	[22]
NiO-BCZYYb Dry pressing	LSCF	BCZYYb	40	118(600 $^{\circ}$ C)	[25]
NiO-BCZYYb One-step phase inversion	LSCF	BCZYYb	40	302 (600 $^{\circ}$ C)	This work

cell performance dominated by ohmic losses in the electrolyte, our power density could be increased to  $430 \text{ mW cm}^{-2}$  by reducing the electrolyte thickness to  $14 \mu\text{m}$ , which is comparable to the highest reported performance in PCFCs with phase inversion anode [22]. It is also emphasized that a distinguishing feature of our approach was the use of a one-step phase inversion method starting from precursors such as carbonates and oxides, which directly form the crystalline phase with the desired microstructure instead of using the crystalline BCZYYb powder as employed in related works [22]. This results in a time and energy-saving method, which has proven beneficial for further development of high-performance PCFCs.

Nyquist plots of impedance data obtained at open circuits of both two single cell were obtained to understand the improvement of the performance, as shown in Fig. 4. There is a slight difference of the intercept in the x-axis due to minor difference in the thickness of the electrolyte, which is consistent with the SEM images shown above. As expected, the increased charge transfer rates are likely due to the finer skin layer with smaller pore size and the increased degree of gas transport speed from the fingerlike pores. In order to separate anode contribution from the overall electrode polarization resistance, an equivalent circuit model analysis was employed. The equivalent circuit used for data fitting is displayed in Fig. S5 where  $R_0$  is the serial resistance due to the electrolyte and connection wires,  $L1$  is the inductance;  $R1$ -CPE1,  $R2$ -CPE2, and  $R3$ -CPE3 are the electrode resistive element corresponding to the high-, mid-, and low frequency arcs, respectively. According to the high-resolution impedance study for anode-supported cells, the arcs in the high-frequency range is associated with anode activation polarization [31]. And the equivalent circuit model analysis confirmed that the reduction in total polarization

resistance originated from the optimized anode structure. Fig. 4c displays the anode polarization resistance comparison between these two cells. It is evident that the improvement of the performance was mainly caused by the anode contribution. The anode polarization resistances from the one-step phase inversion were much smaller than those from traditional dry pressing samples which was similar to the trends observed in the I-V curve.

#### 4. Conclusion

A one-step phase inversion method has been successfully utilized in PCFCs in order to rationally design a new anode microstructure. The finer skin layer provides more active sites for chemical reactions and the fingerlike pores reduce the time required for gas transport. The maximum power density of the single cell with the designed anode was nearly two times higher than the tradition method, from 268, 199, 118 and  $58 \text{ mW cm}^{-2}$  to 491, 402, 302 and  $200 \text{ mW cm}^{-2}$  at 700, 650, 600 and  $550^{\circ}\text{C}$ , respectively. AC impedance data derived from the Nyquist plots indicated that the charge transfer and gas transport resistance exhibited a significant reduction with the phase inversion anode. This was further confirmed by the equivalent circuit model analysis, indicating that the anode contribution to the overall cell performance were decreased in the phase inversion anode, especially at lower temperatures. The one-step phase inversion process towards rational design of anode microstructures demonstrates promise for the fabrication of intermediate temperatures PCFCs.

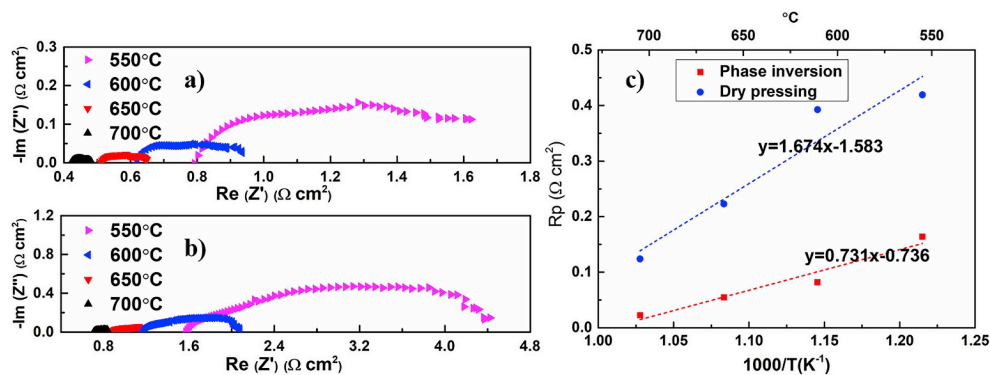


**Fig. 4.** Nyquist plots of impedance measured at open circuits with a) one-step phase inversion anode and b) dry pressing anode and c) anode polarization resistances from Nyquist plots of impedance data of single cells.

## Acknowledgement

KSB was supported in part by an appointment to the National Energy Technology Laboratory Research Participation Program, sponsored by the U.S. Department of Energy and administered by the Oak Ridge Institute for Science and Education. We also gratefully acknowledge the financial support from the Department of Energy, Nuclear Energy Research Program (DOE-NEUP) Project: 17-12798: Nanostructured Ceramic Membranes for Enhanced Tritium Management. KH acknowledges the start-up fund sponsored by Clemson University, and the resources of the Center for Functional Nanomaterials, which is a U.S. DOE Office of Science Facility, at Brookhaven National Laboratory under Contract No. DE-SC0012704.

## Appendix A. Supplementary data

Supplementary data to this article can be found online at <https://doi.org/10.1016/j.jpowsour.2019.02.040>.

## References

- [1] N.Q. Minh, *J. Am. Ceram. Soc.* 76 (1993) 563–588.
- [2] Z. Zhan, S.A. Barnett, *Science* 308 (2005) 844–847.
- [3] S. Park, J.M. Vohs, R.J. Gorte, *Nature* 404 (2000) 265–267.
- [4] S.M. Haile, *Acta Mater.* 51 (2003) 5981–6000.
- [5] S. Chu, A. Majumdar, *Nature* 488 (2012) 294–303.
- [6] K.D. Kreuer, *Annu. Rev. Mater. Res.* 33 (2003) 333–359.
- [7] B. Wang, X. Liu, L. Bi, X.S. Zhao, *J. Power Sources* 412 (2019) 664–669.
- [8] X. Xu, L. Bi, X.S. Zhao, *J. Membr. Sci.* 558 (2018) 17–25.
- [9] Z. Zhu, E. Guo, Z. Wei, H. Wang, *J. Power Sources* 337 (2018) 132–138.
- [10] Y. Chen, S. Yoo, K. Pei, D. Chen, L. Zhang, B. deGlee, R. Murphy, B. Zhao, Y. Zhang, Y. Chen, M. Liu, *Adv. Funct. Mater.* 28 (2018) 1704907.
- [11] B. Hua, N. Yan, M. Li, Y.-F. Sun, Y.-Q. Zhang, J. Li, T. Etsell, P. Sarkar, J.-L. Luo, *Adv. Mater.* 28 (2016) 8922–8926.
- [12] J. An, Y.-B. Kim, J. Park, T.M. Gür, F.B. Prinz, *Nano Lett.* 13 (2013) 4551–4555.
- [13] T. Suzuki, Z. Hasan, Y. Funahashi, T. Yamaguchi, Y. Fujishiro, M. Awano, *Science* 325 (2009) 852–855.
- [14] Z. Zhan, D. Han, T. Wu, X. Ye, S. Wang, T. Wen, S. Cho, S.A. Barnett, *RSC Adv.* 2 (2012) 4075–4078.
- [15] H. Moon, S. Kim, S. Hyun, H. Kim, *Int. J. Hydrog. Energy* 33 (2008) 1758–1768.
- [16] C. Xia, Meilin Liu, *Solid State Ionics* 144 (2001) 249–255.
- [17] N. Yang, X. Tan, Z. Ma, *J. Power Sources* 183 (2008) 14–19.
- [18] W. Sun, N. Zhang, Y. Mao, K. Sun, *J. Power Sources* 218 (2012) 352–356.
- [19] C. Ren, S. Wang, T. Liu, Y. Lin, F. Chen, *J. Power Sources* 290 (2015) 1–7.
- [20] J. Gao, X. Meng, T. Luo, H. Wu, Z. Zhan, *Int. J. Hydrog. Energy* 42 (2017) 18499–18503.
- [21] Z. Zhu, Y. Cao, X. Dong, X. Meng, Y. Zhao, Z. Ding, Z. Wei, *Int. J. Appl. Ceram. Technol.* 15 (2018) 1567–1576.
- [22] N. Shi, F. Su, D. Huan, Y. Xie, J. Lin, W. Tan, R. Peng, C. Xia, C. Chen, Y. Lu, *J. Mater. Chem. A* 5 (2017) 19664–19671.
- [23] J. Zhu, G. Zhang, G. Liu, Z. Liu, W. Jin, N. Xu, *Adv. Mater.* 29 (2017) 1606377.
- [24] J. Martynczuk, M. Arnold, H. Wang, J. Caro, *Adv. Mater.* 19 (2007) 2134–2140.
- [25] J. Gao, Y. Meng, S. Lee, J. Tong, K.S. Brinkman, *JOM* (2018) 1–6.
- [26] M. Shang, J. Tong, R. O'Hayre,  $\text{BaCo}_{0.4}\text{Fe}_{0.4}\text{Zr}_{0.2}\text{O}_{3-\delta}$ , *RSC Adv.* 3 (2013) 15769–15775.
- [27] S. Lee, S. Park, S. Wee, H. woo Baek, D. Shin, *Solid State Ionics* 320 (2018) 347–352.
- [28] T. Onishi, D. Han, Y. Noda, N. Hatada, M. Majima, T. Uda, *Solid State Ionics* 317 (2018) 127–135.
- [29] C. Duan, J. Tong, M. Shang, S. Nikodemski, M. Sanders, S. Ricote, *Science* 349 (2015) 1321–1326.
- [30] J. Xiao, W. Sun, Z. Zhu, Z. Tao, W. Liu, *Mater. Lett.* 73 (2012) 198–201.
- [31] A. Leonide, V. Sonn, A. Weber, *J. Electrochem. Soc.* 155 (2008) B36–B41.